I&EC research
Industrial & Engineering Chemistry Research

Article

Cite This: Ind. Eng. Chem. Res. 2019, 58, 2084−2098

pubs.acs.org/IECR

Investigation of Bubbling Behavior in Deep Fluidized Beds at Different Gas Velocities using Electrical Capacitance Tomography

Cornelius E. Agu,*[,†] Ambrose Ugwu,[‡] Christoph Pfeifer,[§] Marianne Eikeland,[†] Lars-Andre Tokheim,[†] and Britt M. E. Moldestad[†]

[†]Department of Process, Energy and Environmental Technology, University College of Southeast Norway, 3918 Porsgrunn, Norway
[‡]Department of Energy and Process Engineering, Norwegian University of Science and Technology, 7491 Trondheim, Norway
[§]Department of Material Sciences and Process Engineering, University of Natural Resources and Life Sciences, 1190 Vienna, Austria

ABSTRACT: Deep bubbling fluidized beds have some advantages that make them attractive for industrial applications. Using different powders, this paper investigates the bubbling behavior in deep beds. The results show that bubbles grow faster in the bed of angular/rough particles than in that of round/smooth particles and that the rate of bubble growth increases with increase in the particle size. With an increase in the bed height, the changes in the bubble diameter and solids distribution decrease within the bubbling regime but may vary within the slugging regime due to the chaotic behavior of slug flows. The bubble frequency increases with an increase in the gas velocity only when the bubble diameter is below a certain threshold value; for larger bubbles, the bubble frequency is lower. The maximum bubble frequency indicates the onset of slugging. Correlations for predicting the maximum bubble/slugging frequency averaged over the bed height and the corresponding bubble diameter are proposed.

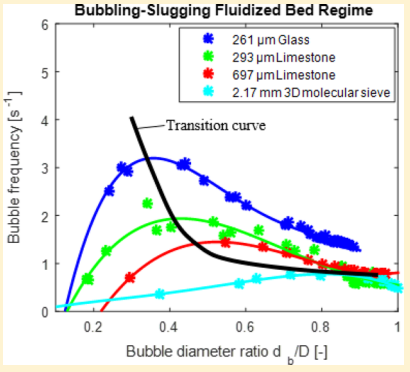

1. INTRODUCTION

The application of bubbling fluidized beds covers a wide range of bed aspect ratios (ratio of bed height to bed diameter), but several studies have been focused mainly on beds with aspect ratios slightly above unity, usually within the range of 1−2. This is possibly because the behavior in freely bubbling beds with such aspect ratios can be analyzed using simple theories and physics such as the two-phase theory proposed by Toomey and Johnstone.[1] Studies have also shown that in such shallow beds bubbles do not grow into slugs but instead transit into the turbulent fluidization regime as the gas velocity increases. Bubbles can develop into slugs when the bed height is larger than twice the bed diameter.[2] Baeyens and Geldart[3] proposed models that describe the maximum bed height below which a freely bubbling behavior is guaranteed and the bed height above which the slug flow can be stable as given in eqs 1 and 2, respectively, where h_0 [cm] is the height of the bed in fixed state and D [cm] is the bed diameter.

$$\frac{h_0}{D} = 60D^{-0.175} \tag{1}$$

$$\frac{h_0}{D} = \frac{(1 - 2.51D^{-0.8})}{0.13D^{0.47}} \tag{2}$$

When the aspect ratio is greater than 2, the bed is usually described as a deep bed. With the same bed diameter, an increase in the aspect ratio results in an increase in the pressure drop over the bed. For the application of fluidized beds in chemical reactors, the basic requirement is to provide adequate heat for reactions, particularly in thermochemical processes, and to increase the reactant contact time and surface area while ensuring uniform temperature and material distribution. Provided that the bed is in the bubbling regime, a proper heat and material distribution within the bed can be achieved. With increasing bed pressure drop, the gas residence time increases. In addition, due to flow of well-established bubbles, the circulation of solids at increasing gas velocity is more vigorous in a deep bed than in a shallow bed.[4] However, the advantage of using a deep bed especially in laboratory and pilot scales is limited to the critical gas velocity above which slugs begin to appear in the bed. In most fluidized bed applications, slugging is avoided as a mode of contact due to the possibility of gas escaping with the slugs. The slugs usually separate gas from the solid particles in the bed, reducing the contact area and time for the reacting species.

The aim of this study is to investigate the behavior of bubble flow through a deep bed at different gas velocities and bed heights. Few studies are available on the chosen topic,[5] although there are numbers of related studies. In a computational study, Wang et al.[6] investigated the effect of non-spherical particles on the bubbling behavior in a bed of aspect ratio 12 and concluded that bubbles move with higher degree of fluctuation compared with those in a bed of spherical particles. Using CFD computations, Verma et al.[7] found that bubble size increases only within a certain range of different

Received: October 10, 2018
Revised: January 8, 2019
Accepted: January 11, 2019
Published: January 11, 2019

DOI: 10.1021/acs.iecr.8b05013
Ind. Eng. Chem. Res. 2019, 58, 2084−2098

bed diameters and then remains constant. An increase in a bed diameter at a constant bed height indicates a decrease in the aspect ratio. The study[7] was focused mainly on shallow beds where the highest bed aspect ratio investigated was 2.0. In a similar study using ultrafast electron beam X-ray tomography in beds with aspect ratio limited to 2.0, Verma et al.[8] concluded that there is no significant difference in the bubble characteristics with changes in the bed aspect ratio. Laverman et al.[9] investigated the effect of bed aspect ratio and bed diameter in a freely bubbling bed using a 2-D particle image velocimetry, and their results show that bubble sizes hardly depend on the bed height within the experimental error but are affected by the bed diameter. In addition, the slug flow behaviors in deep fluidized beds have also been investigated in different studies.[10,11] In a bed of diameter 76.2 mm and height 40.0 cm containing 1.5 mm spherical iron oxide particles, Wang et al.[10] showed that at lower gas velocities bubbles flow freely but at higher gas velocities above the minimum slugging velocity the bed slugs. The slug rise velocity increases with an increase in the gas velocity but at nearly the same frequency of 1 Hz. A similar value for the limiting slug frequency was also observed in Cho et al.,[11] where polyethylene particles of size 603 μm were fluidized in a bed of diameter 7.0 cm and aspect ratio 5.3. The setup used in Cho et al.[11] was designed to simulate the dimensional similarity of a commercial fluidized bed reactor, indicating that the behavior observed in their study can be scaled up to a larger bed.

As there have not been many experimental works on the behavior of a deep fluidized bed at increasing gas velocity, this study focuses on the measurement and analysis of bubble behavior at different gas velocities. The analysis is based on the radial distribution of the solids fraction and on the bubble properties such as bubble size and bubble frequency, which are among the parameters that give an indication about the behavior of fluidized beds.[4] Although slugging behavior is peculiar to small and pilot-scale fluidized bed reactors, Raghuraman and Potter[12] showed that it can also be expected in some large scale reactors depending on the bed aspect ratio. Therefore, for in-depth characterization of behavior in deep beds, a small-scale fluidized bed column is used in this study. In the experimental setup, the bubble properties are determined by analysis of the solids fraction obtained with a dual-plane electrical capacitance tomography (ECT) at ambient temperature and pressure. ECT is used to measure the relative permittivity between two nonconducting phases, and being a nonintrusive sensor, it does not interrupt the flow or bed it measures. Previous studies[13,14] confirmed that this measurement technique provides bubble diameters that compare well with bubble sizes obtained with other techniques. In the subsequent sections, the experimental procedure is presented. The results, which include effects of bed height, material, and particle size on bubble properties and solids distribution, are discussed.

2. PREDICTION OF BUBBLE PROPERTIES

Several models described in the literature can predict bubble properties, including the bubble size and bubble rise velocity. For this study, the bubble diameter and bubble frequency are considered the most relevant. There are only a few correlations[15,16] available for the bubble frequency. The bubble diameter can be predicted using a number of different correlations.[17−20] However, the review of Karimipour and Pugsley[21] showed that the models given by Choi et al.[17] and Mori and Wen[18] give the best results for Geldart B solids.[22] The Choi et al. model is described as follows:

$$(U_0 - U_{mf})[d_b - d_{b0c} - 1.132h] + 0.474g^{0.5}(d_b^{1.5} - d_{b0c}^{1.5}) = 0 \quad (3)$$

where, d_b [cm] is the bubble diameter at a position h [cm] from the bottom of the bed, U_0 [cm/s] is the superficial gas velocity, U_{mf} [cm/s] is the particle minimum fluidization velocity, and g [cm/s^2] is the acceleration due to gravity. The initial bubble diameter d_{b0c} [cm] is obtained from

$$d_{b0c} = \frac{1.63}{g^{0.2}}[A_0(U_0 - U_{mf})]^{0.4} \quad (4)$$

where A_0 is the catchment area [cm^2] defined as the area of a distributor plate per hole. For a porous plate, $A_0 \approx 0.56$ cm^2 as described in Darton et al.[19]

The bubble diameter based on Mori and Wen[18] can be obtained from eqs 5 and 6.

$$d_b = 0.652[A(U_0 - U_{mf})]^{0.4} - (0.652[A(U_0 - U_{mf})]^{0.4} - d_{b0m})\exp\left(-0.3\frac{h}{D}\right) \quad (5)$$

$$d_{b0m} = 0.00376(U_0 - U_{mf})^2 \quad (6)$$

Again, d_b, h, and D are in [cm], U_0 and U_{mf} are in [cm/s], and $A = \frac{1}{4}\pi D^2$ is the bed cross sectional area. Here, d_{b0m} is the initial bubble size near the surface of a porous plate distributor.

3. EXPERIMENTAL PROCEDURES

3.1. Experimental Setup. The experimental setup is similar to that described in Agu et al.[23] As shown in Figure 1, the setup consists of a cylindrical column with a 10.4 cm

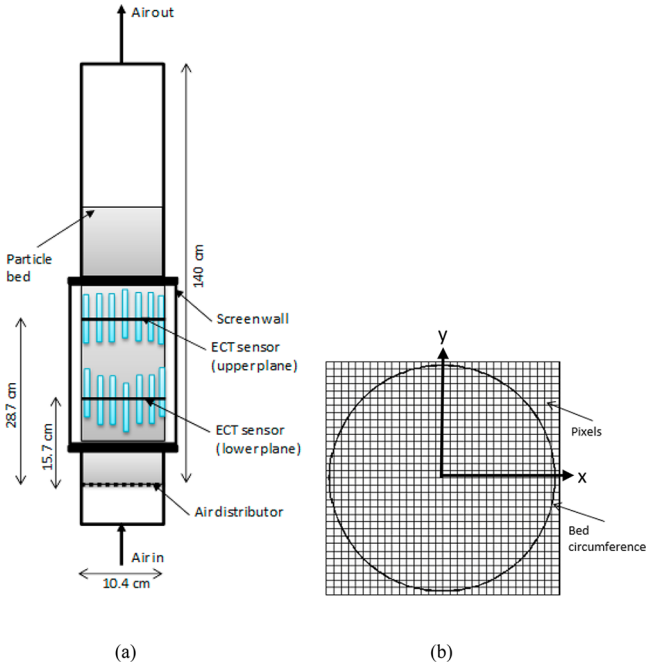

Figure 1. (a) Cold fluidized bed using dual-plane ECT sensors for measurement of solids fraction distribution. (b) Cross section of the bed divided into 32 by 32 pixels in the x and y directions, respectively.

DOI: 10.1021/acs.iecr.8b05013
Ind. Eng. Chem. Res. 2019, 58, 2084−2098

internal diameter and 1.4 m height. The column is fitted with a porous plate distributor and twin-plane ECT sensors located at 15.7 and 28.7 cm from the distributor. The porous plate is made of highly porous sintered stainless steel material and has a diameter of 10.8 cm, thickness of 3 mm, and a porosity of 40%, corresponding to a flow area of 36.6 cm^2. Figure 2 shows

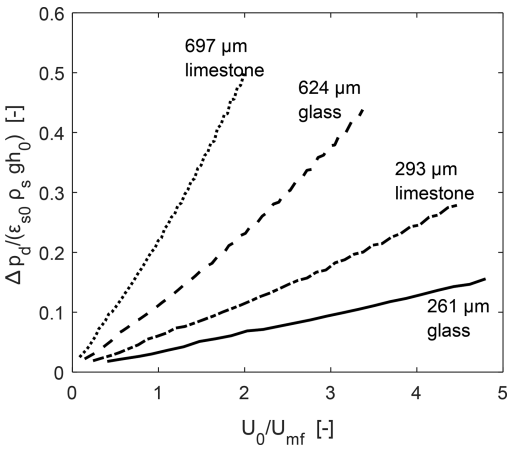

Figure 2. Ratio of pressure drop across a porous plate to pressure drop over different beds. Δp_d is the pressure drop across the distributor, and $\varepsilon_{s0}\ \rho_s\ gh_0$ is the mean bed pressure drop.

the pressure drop across the distributor plate at different gas velocities compared with the pressure drop in the bed of different particles. Each of the ECT sensors consists of 12 electrodes, uniformly distributed around the plane circumference on the outer wall of the bed column. The sensors are shielded against external field effects. The cross section of each sensor is divided into 32 × 32 square pixels, of which 812 pixels lie within the bed as shown in Figure 1(b). Each pixel holds a normalized relative permittivity between 0 and 1, denoting the gas and solids concentrations, respectively. The ECT sensors were calibrated prior to use for a given powder. To minimize the signal-to-noise level, the solid particles forming the bed were uniformly filled across the measurement planes during the calibration. In operation, ECT measures the capacitance value between every pair of electrodes around the bed. The maximum rate at which the ECT sensors acquire information from the bed is 100 frames per second. The Linear Back Projection reconstruction algorithm[24] is applied to obtain the distribution of relative permittivity of the dense material from the ECT data.

In this study, different powders were investigated. The powders include limestone particles with two different mean particle sizes, glass particles with three different particle sizes, and sand and molecular sieve particles. The Z10-02 molecular sieve manufactured and supplied by Zeochem AG is used for gas adsorption. Including this powder increases the range of particle sizes covered in this study. Table 1 shows the particle properties of all the powders, where ρ_s is the particle density obtained with a gas pycnometer and d_s is the mean particle size obtained from the sieve analysis. The solids fraction ε_{s0} at a fixed state was obtained from $\varepsilon_{s0} = m/(\rho_s A h_0)$, where m is the mass of solids charged into the bed. The round (spherical) particles are also smooth in texture, while the angular (nonspherical) particles are rough in texture. As can also be seen in Table 1, these different particle types belong to a wide range of solid classes (Geldart[22] classification) ranging from small Geldart B to large Geldart D solids. The chosen range of particle sizes is widely applied in fluidized bed reactors. For example, the size of particles in the Geldart BD or D group is used in fluidized bed combustors to minimize particle entrainment, while in biomass gasifiers particle size in the B group is often used due to lower the gas velocity involved. To demonstrate the effect of bed height on the bed behavior, the three powders with smaller particle sizes were used since for larger particles the minimum slugging velocity is less dependent on the bed height,[3] indicating that the effect of bed height on bubble size may be insignificant for larger particles. For each of the three smaller powders, the bed heights applied were 52, 58, and 64 cm, and for the other powders, the bed height was in the range of 40−60 cm. The corresponding aspect ratios for all the bed heights lie between 3.9 and 6.2, which are within the range of 1.6−8.7 calculated from eqs 1 and 2 for flow of unstable slugs in the bed.

The experiments were carried out using compressed air supplied through a root blower. The maximum flow rate and pressure drop across the air blower are 120 m^3/h and 0.15 bar(g) at the ambient temperature, respectively. The air velocity was varied at an increasing step within the range given in Table 2. For each powder, Table 2 also shows the minimum fluidization velocity and the minimum slugging velocity obtained in this study by the method described in Agu et

Table 2. Gas Velocities Investigated with Minimum Velocities at Flow Regimes

Materials	Mean particle diameter [μm]	Minimum fluidization velocity [cm/s]	Minimum Excess velocity at slugging [cm/s]	Superficial air velocity [cm/s]
Glass	188	3.80	10.7	1.0−27.5
Glass	261	8.15	6.54	3.9−33.4
Glass	624	23.20	10.60	15.7−53
Limestone	293	13.80	7.36	3.9−37.3
Limestone	697	39.24	9.76	35−76.5
Sand	483	16.50	9.32	11.8−43
Molecular sieve	2170	76.85	14.72	68.6−102

Table 1. Bed Materials Investigated with Their Properties

Materials	Size range [μm]	Solid class	Shape	ρ_s [kg/m^3]	d_s [μm]	ε_{s0} [-]
Glass	100−550	B	round	2500	188	0.63
Glass	100−550	B	round	2500	261	0.62
Glass	450−900	BD	round	2500	624	0.62
Limestone	150−450	B	angular	2837	293	0.51
Limestone	450−1100	BD	angular	2837	697	0.48
Sand	300−700	B	angular	2650	483	0.55
Molecular sieve	1600−2600	D	round	1300	2170	0.62

DOI: 10.1021/acs.iecr.8b05013
Ind. Eng. Chem. Res. 2019, 58, 2084−2098

al.[23] At a given air velocity, the images of the solids distribution at the measurement planes were captured and recorded for 60 s at a frequency of 100 Hz, the same as the maximum rate of measurements with the ECT sensors. The recorded image data were exported for analysis in MATLAB.

As described in Agu et al.,[25] Figure 3 shows the distribution of solids fraction obtained in the bed of 261 μm glass particles

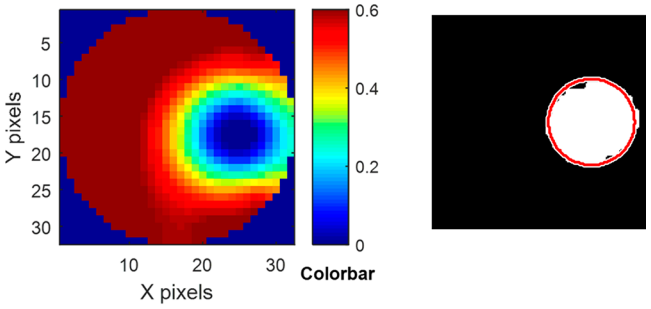

(a) (b)

Figure 3. Behavior in the lower plane of the bed of 261 μm glass particles. (a) Distribution of solids volume fraction as indicated by the numbers in the color bar. (b) Actual bubble region (white) and approximately spherical bubble (region bounded by a red circle).

at a 35th s of 0.147 m/s airflow. The higher values on the figure color bar indicate higher solid concentrations. In the regions where the solid concentration approaches zero, bubbles can be observed. As bubbles have been found to contain a certain amount of solids,[4] any region bounded by the solids fraction between 0 and 0.2 is considered as a bubble in this study. Using this bubble-solid threshold, different bubbles are identified. The sensitivity of bubble properties to a change in the threshold value decreases with increasing gas velocity and particle sphericity. Within the bubbling regime, a change in the cutoff solids fraction to a value within 0.15−0.25 (corresponding to ±25% change) results in a change in the bubble diameter within 5% to 7% for the round particles and 6% to 10% for the angular particles. Despite the bubble-solid threshold value, analysis of the image data reveals that only a single bubble can be mostly observed in each plane at every gas velocity as shown in Figure 3. This is probably due to the small size of the bed diameter, which may enhance the lateral bubble coalescence and due to the location of the ECT sensors (15.7 and 28.7 cm) before which the number of rising bubbles must have been reduced due to axial coalescence. However, the activities of a single bubble can be traced easily, making the data analysis less cumbersome. For every bubble identified in this analysis, its properties are calculated using the "image processing toolbox" in MATLAB. The number of pixels occupied by a bubble at any given time is obtained and mapped into the actual bubble projected area based on $A_b = A\left(\frac{N_b}{N_{pix}}\right)$, where N_b is the number of pixels occupied by the bubble and N_{pix} = 812 is the total number of pixels within the plane. The changes in the values of A_b with time are used to obtain the bubble frequency as described in the next section.

Figure 4 shows the sketch of a typical profile of the projected bubble area at a given plane that can be observed during the bubble passage. As can be seen, the projected area gradually increases from zero, reaching a peak value and then gradually

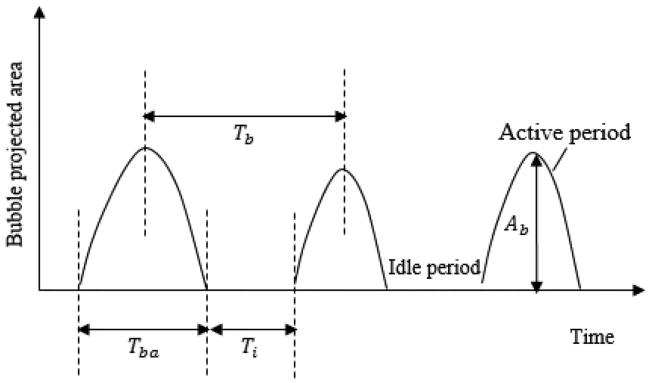

Figure 4. Sketch of the time evolution of the bubble projected area typical for a bubbling fluidized bed, where T_{ba} is the average active bubble period, T_i the average idle period, T_b total bubble period, and A_b the average bubble cross sectional area.

decreases to zero. After the observed projected area is reduced to zero, the bed becomes idle (free from bubble) until the next active period. The gradual increase and decrease in the projected area during the active period is evidence that the bubble is spherical or oval in shape. The peak of the projected area during the bed active period corresponds to the cross-sectional area at the center of the bubble.

To verify the repeatability of the experiment, five different measurements were taken at intervals of 2 min for each air velocity. These five data sets were analyzed separately, and their average was taken to reduce the random error associated with the measurements. For all the beds, the mean variation in the measurements when the experiment is repeated a number of times is less than 2.5%.

3.2. Measurement of Bubble Properties. The bubble diameter in each plane is obtained as the time-averaged diameter of an equivalent sphere having the same projected area as the bubble. As shown in Figure 4, the bubble diameter can be based on the peak projected area assuming a spherical bubble.

$$d_b = \frac{1}{n}\sum\left(\sqrt{\frac{4A_{b,i}}{\pi}}\right) \tag{7}$$

Here, n is the number of times over the measurement period when full bubble passages are observed in the plane, and $A_{b,i}$ is the peak of the projected areas observed in the plane at each bubble passage.

As the bubble activity in each plane is cyclic, Figure 4 shows that it is possible to record the time at which a bubble arrives at a plane and the time at which the next bubble arrives at the same plane. The time interval between the arrivals of two successive bubbles is referred to as the bubble period. For the single bubble observed at every gas velocity, the inverse of the bubble period T_b is described as the bubble frequency, f_b.

$$f_b = \frac{1}{T_b} \tag{8}$$

4. RESULTS AND DISCUSSION

The four different materials considered in this study have different properties that can influence the behavior of a fluidized bed. For example, in addition to the difference in their densities, limestone particles are cohesive and irregular in

DOI: 10.1021/acs.iecr.8b05013
Ind. Eng. Chem. Res. 2019, 58, 2084−2098

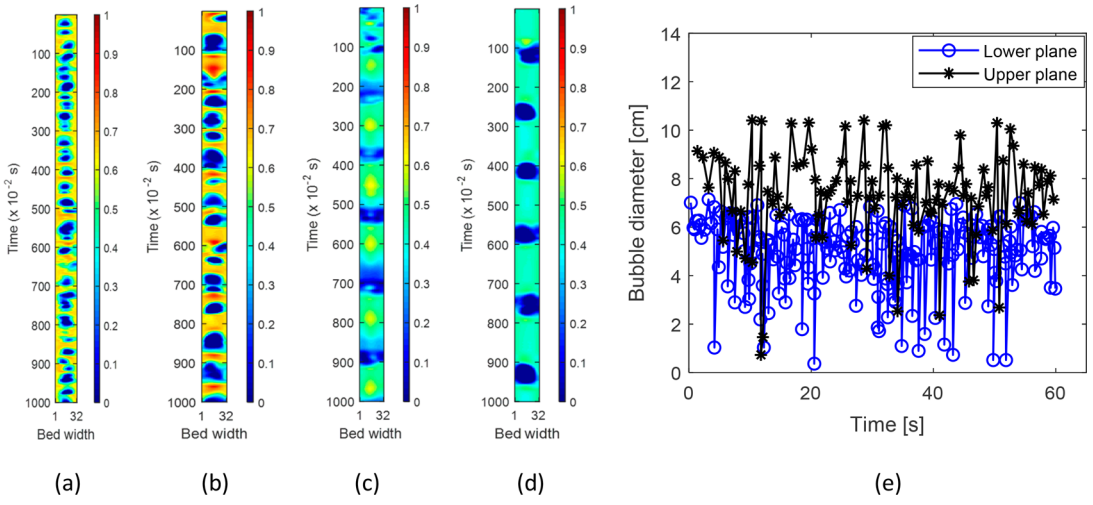

Figure 5. Images for the first 10 s of the flow in beds of 261 μm glass at 0.177 m/s [(a) lower plane and (b) upper plane] and 293 μm limestone at 0.235 m/s [(c) lower plane and (d) upper plane], where the horizontal axis is the position on a line through the bed cross section. Solids fraction increases with the color scale value. (e) Temporal variation of bubble diameter in the lower and upper planes of the glass particles. Bed aspect ratio: 5.6.

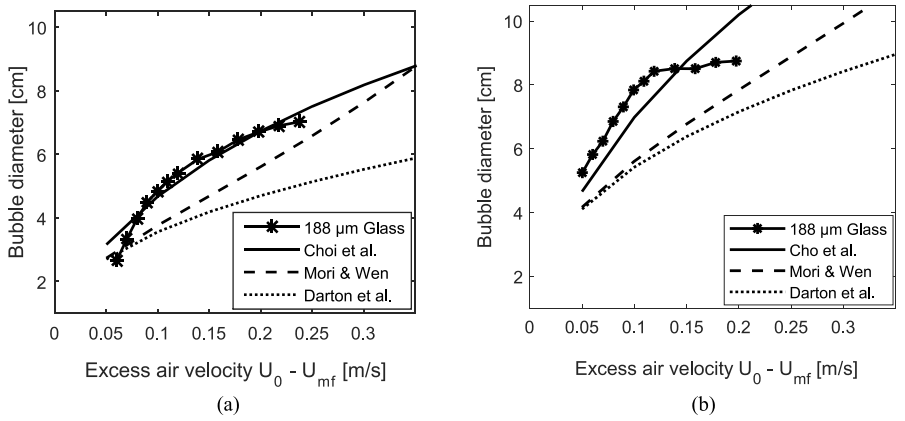

Figure 6. Bubble diameters measured in the bed of 188 μm glass particles compared with the values computed from different correlations: (a) lower plane and (b) upper plane. Bed height = 52 cm.

shape, whereas glass particles are noncohesive and regular in shape. Of all these materials, limestone and glass are the two extremes. Sand particles are rough but not as cohesive as limestone particles, while the molecular sieve particles are smooth and spherical in shape but porous unlike the glass particles. These properties are explored in this study to investigate their effects on the bubbling behavior. Figure 5 compares the bubble behavior in the bed of 293 μm limestone with that in the bed of 261 μm glass particles at about the same excess gas velocity $U_0 - U_{mf}$, 0.097 and 0.095 m/s, respectively. For the bed of glass particles, bubbles rise more frequently in the lower plane (15.7 cm above the distributor), but as they coalesce in the axial direction while moving up to the upper plane at 28.7 cm above the distributor, the rise frequency decreases. This behavior is typical of particles of good fluidity.[4] For the bed of limestone particles, a different behavior can be observed in the two different planes. The bubble frequency in the two planes is almost the same after 1 s. In the lower plane, bubbles spread across the bed and coalesce to form a flat face bubble similar to those at high velocity in Geldart D solid beds. However, Figure 5(d) shows that as the bubbles rise up the bed, splitting and coalescence result in a round face bubble that sticks to the wall, a behavior peculiar to fine rough particles at high gas velocity.[9] In addition to the particle properties, this nonuniform bubbling behavior over the bed of limestone particles may also be attributed to segregation, where the larger particles move down and the smaller particles move up the bed due to bubble passage. Moreover, since the gas velocity $U_0 - U_{mf}$ is higher than that at the minimum slugging condition as shown in Table 2, there are flows of slugs in both beds, though at this moderate gas velocity, the flows of slugs is not continuous as can be seen in Figure 5(e). When slugs flow, the bubble diameter is close to the bed diameter. Between two successive slugs, the bed bubbles freely. There is no slug flow in the lower plane, but the impact of the flow of slugs in the upper plane can still be seen in the planes below. The complete passage of slugs leads to a sudden drop in the bubble diameter at both planes due to escape of gas which results in a temporal higher concentration of solids in the bed.

4.1. Measured versus Predicted Bubble Diameter. Most correlations available in the literature provide bubble volume-equivalent diameter, which has been considered as the true bubble diameter. In this study, the method for measuring the bubble diameter using 2D ECT data is based on the maximum projected bubble area during each bubble passage

DOI: 10.1021/acs.iecr.8b05013
Ind. Eng. Chem. Res. 2019, 58, 2084−2098

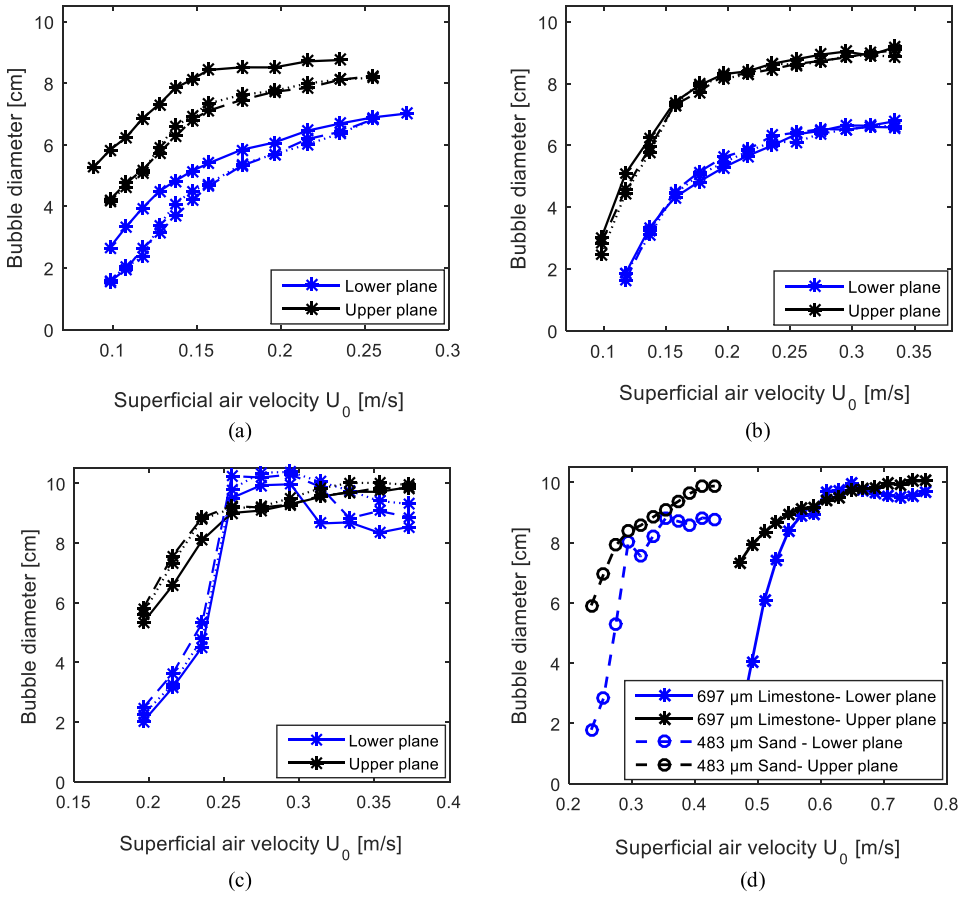

Figure 7. Bubble diameter against superficial gas velocity for (a) 188 μm glass particles, (b) 261 μm glass particles, and (c) 293 μm limestone particles at different aspect ratios h_0/D. Lines: solid, h_0/D = 5; dashed, h_0/D = 5.6; and dotted, h_0/D = 6.2, and for (d) 697 μm limestone and 483 μm particles comparing their behavior with that of 293 μm limestone particles.

assuming a spherical bubble. However, a more realistic bubble size based on ECT measurements can also be obtained by integrating the product of the projected bubble area and bubble velocity with respect to time. The average bubble velocity over a bed height can be calculated from the time it takes a bubble to pass from one plane to another. This method, however, may be limited by the spacing between the measurement planes. As observed in this study, bubbles become larger before reaching the upper plane due to coalescence, especially in the bubbling regime, making it difficult to determine the time it takes a bubble to pass through the two planes by any technique such as the cross-correlation technique. With the use of ECVT (electrical capacitance volume tomography), the bubble volume-equivalent diameter has been obtained by different researchers,[26] with some indications that the measured bubble diameter can be larger than the bed diameter, showing that bubbles are nonspherical in shape when they are large due to wall effects. Figure 6 compares the bubble diameter measured in this study with those obtained from the correlations given by Choi et al.,[17] Mori and Wen,[18] and Darton et al.[19] For the same value of $U_0 - U_{mf}$, the results show that the bubble diameter is larger in the upper plane. The bubble diameter increases with an increase in the excess air velocity except when the bubble (slug) size approaches the bed diameter as can be seen in the upper plane. On average, the trend of the experimental data is the same as those obtained from the three different bubble diameter models. The predictions given by Choi et al. agree well with the bubble diameter measured in the lower plane over the entire range of excess velocity and with that obtained in the upper plane up to the excess velocity of 0.15 m/s. Over the range of velocities shown, the two other models underpredict the experimental data in both planes, but the predictions given by the Mori and Wen correlation are better than those obtained from the Darton et al. model. Moreover, none of the correlations predict the behavior in the slugging regime, where the excess gas velocity is greater than that corresponding to the minimum slugging velocity as given in Table 2. This is probably because these models are developed for a freely bubbling bed. Although the Choi et al.[17] model still predicts the bubble diameter with a good accuracy even in the slugging regime where $U_0 - U_{mf} > 0.107$ m/s, particularly in the lower plane it should be noted that the slug flow is not continuous, and it starts from the upper part of the bed as shown in Figure 5(e). The extent to which the flow of slugs covers the bed height depends on the gas velocity and particles. For this smaller particle size, 188 μm, the lower plane bubbles freely at all gas velocities in the range shown in Figure 6 due to low bubble growth rate. At the upper plane, the bed slugs but not continuous. Since the bubble diameter presented in this study is the time-averaged value as given in eq 7, the bubble diameter depends on the most frequent value recorded between the bubbling and slugging regimes over the measurement period. Increasing the gas velocity increases the chances of slug flow over time. However, this behavior is peculiar to fine and smooth particles. For rough (angular) or large particles, the

DOI: 10.1021/acs.iecr.8b05013
Ind. Eng. Chem. Res. 2019, 58, 2084−2098

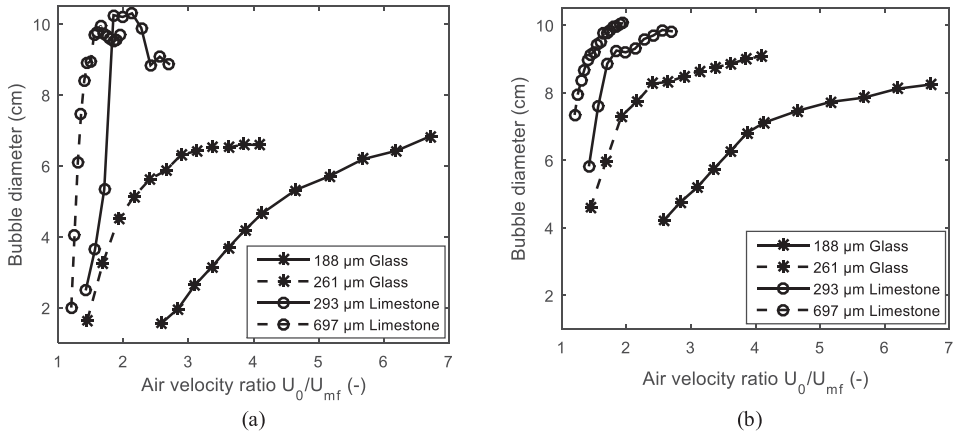

Figure 8. Variation of bubble diameter with the gas velocity ratio, showing the influence of particle sizes on bubble growth: (a) lower plane and (b) upper plane. Bed height = 58 cm.

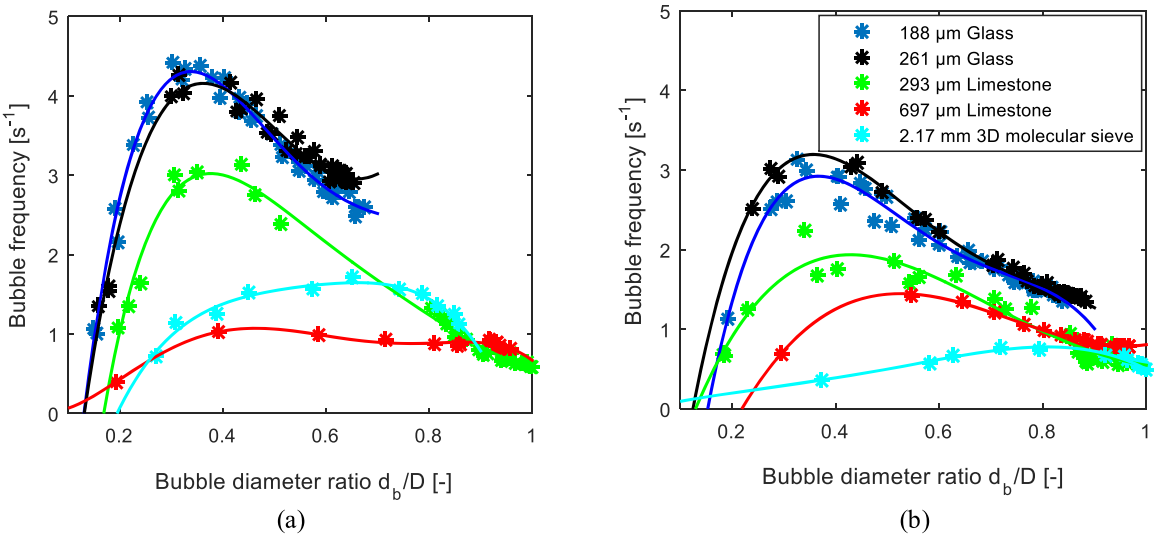

Figure 9. Bubble frequency curve based on bubble diameter, showing the minimum slugging condition at the peak of the curve: (a) lower plane and (b) upper plane.

occurrence of slugs over time and along the bed axis dominates, leading to a larger bubble diameter than that predicted by the Choi et al. model as can be seen in the subsequent sections. The bed of 188 μm glass particles at an initial height of 52 cm is used in this demonstration since it provides results, which are in closest agreement with at least one of the bubble diameter correlations in the literature.

4.2. Effect of Bed Height on Bubble Diameter. The variation of bubble diameter with initial bed height is shown in Figure 7 for the three different powders with smaller particle sizes. As can be seen, changes in the bed height have no significant effect on the bubble diameter for the bed of 261 μm glass particles. Between the higher bed heights h_0/D = 5.6 and 6.2, the respective bubble diameters are also the same for the beds of 188 μm glass and 293 μm limestone particles. However, when the bed height is reduced to h_0/D = 5, the corresponding bubble diameter significantly increases for the bed of 188 μm glass and slightly decreases for the bed of 293 μm limestone particles. This effect is more significant in the upper plane for both powders but seems to decrease at increasing gas velocity. Within the bubbling regime, $U_0 < U_{ms}$, the results in general show that for $h_0/D > 5$ the increase in the bed height has a negligible effect on the bubbling behavior. However, at a higher gas velocity, the behavior may be different due to the chaotic behavior of slug flows, especially in the bed of angular particles as shown in Figure 7(c). Figure 7(c) also suggests that when $U_0 > U_{ms}$, the occurrence of slugs dominates in both planes. Within the gas velocity 0.25−0.3 m/s, the predominant flat face slugs, which spread across the bed diameter, flow in the lower plane, while wall slugs rise over the upper plane, resulting in the difference in the bubble diameter seen in this figure. At a higher gas velocity, the wall slugs become dominant in both planes. The wall slugs are smaller than the flat slugs, and as they flow up the bed, coalescence takes place. This behavior can also be seen in the bed of 697 μm limestone particles and to some extent in the bed of sand particles as shown in Figure 7(d). The 624 μm glass and the molecular sieve particles have similar behavior as those of the two smaller glass particles due to the similarities in their shapes and texture.

4.3. Effect of Particle Size on Bubble Diameter. As shown in Figure 5, bubble behavior can be influenced by the particle properties. Based on the two glass powders with smaller particle sizes and the two limestone powders described in Table 1, the influence of material and particle size on bubble diameter can be seen when the bubble diameter is plotted

DOI: 10.1021/acs.iecr.8b05013
Ind. Eng. Chem. Res. 2019, 58, 2084−2098

against the gas velocity ratio U_0/U_{mf} as presented in Figure 8. The value of U_0/U_{mf} measures the degree of bed expansion due to flow of gas at velocity above that required for minimum fluidization as can be seen in eq 9, where $\Delta e = (H_f - H_{mf})/H_{mf}$ is the degree of bed expansion and ε_{mf} is the bed voidage at the minimum fluidization condition. Equation 9 can be derived assuming that the gas residence time and mass of solid particles remain the same at any given gas velocity.

$$\Delta e = \varepsilon_{mf}\left(\frac{U_0}{U_{mf}} - 1\right) \tag{9}$$

Figure 8 shows that the bubble diameter increases with an increase in the gas velocity ratio U_0/U_{mf}, but the rate of this increase varies between the two materials. Bubbles grow faster in the beds of limestone particles than in those of glass particles. This low resistance to bubble growth in the bed of limestone particles can be attributed to higher bed porosity due to low particle sphericity. As given in Table 1, all the angular (nonspherical) particles have a lower solids volume fraction compared to the round (spherical) glass and molecular sieve particles. The lower initial solids fraction indicates that the bed is more porous and will offer a lower resistance to gas and bubble flows. The rate of increase in the bubble size with U_0/U_{mf} also increases with the particle size in both planes. This behavior may also be attributed to the variation in the resistance to gas flow between the different particle sizes. As the particle size increases, the number of particles per unit volume of the bed decreases, resulting in a lower flow resistance. The higher bubble growth rate indicates that slugs can form easily in the fluidized beds of larger particle sizes. For the limestone particles where the bubble diameter is already closer to the bed diameter in both planes at a higher gas velocity, $U_0/U_{mf} > U_{ms}/U_{mf}$, any section above the upper plane will have the same bubble diameter as close as the bed diameter.

4.4. Effect of Particle Size on Bubble Frequency. Figure 9 shows the bubble frequency against the bubble diameter normalized with the bed diameter. For the particles 188 μm glass, 261 μm glass, and 293 μm limestone, the plots include the data from the three different initial bed heights: 52, 58, and 64 cm. As can be seen, the bubble frequency increases with an increase in d_b/D when the bubble diameter ratio is below a certain value $(d_b/D)_M$. At a value of $(d_b/D)_M$, the bubble frequency is maximum. Beyond $(d_b/D)_M$, the bubble frequency decreases with an increase in the bubble diameter. Since bubble diameter increases as gas velocity is increased, this implies that the bubble frequency increases with an increase in the gas velocity until a peak value and thereafter decreases with a further increase in the gas velocity. The bubble frequency increases due to a higher rate of increase in the bubble rise velocity as the gas velocity increases.[27] At higher gas velocities, when the bubble size approaches that for slugs to flow in the bed, the rate of bubble rise velocity becomes lower. This thus increases the time at which bubbles are observed at a given plane, thereby decreasing the bubble frequency. The peak frequency decreases with an increase in the particle size and from the lower to the upper plane, a behavior which has been similarly observed in the previous studies.[26,28] Since the bubble frequency decreases continuously after the peak value, it shows that the local peak frequency denotes the point of local incipient slugging.

The corresponding value of $(d_b/D)_M$ in each plane defines the local minimum bubble size at which a slug begins to flow in the bed. As shown in the figures, $(d_b/D)_M$ increases along the vertical axis of the bed and with increasing particle size. The bubble diameter at the peak frequency is larger in the upper plane due to bubble coalescence. For the powders shown, $(d_b/D)_M$ is in the range of 0.34−0.7 in the lower plane and 0.38−0.8 in the upper plane. Since the peak bubble frequency corresponds to the point at the local onset of slugging, these results show that slugs will be observed in most beds when the ratio of the bubble diameter to the bed diameter is within 0.34−0.8. The results also agree with the findings of Werther.[29] In a 10 cm bed of fine particles with mean diameter 83 μm, Werther[29] observed that slugs begin to flow when $d_b/D \approx 0.33$, and at this minimum slugging condition, the bubble velocity is at its maximum value. However, as the value of $(d_b/D)_M$ depends on the vertical position in the bed, a wider range of bubble diameters at the peak frequency can also be obtained in the fluidized beds. Figure 9 also shows that for the large or angular particles, the bubble/slug frequency reduces to a value closer to or less than 1.0 s^{-1} when the bubble diameter approaches the bed diameter as also observed in other studies.[10,11] However, for the small and smooth particles, the limiting bubble/slug frequency may be over 1.0 s^{-1} as can be seen in Figure 9(b).

4.5. Maximum Slugging Frequency. Similar to the superficial gas velocity U_{ms} at the onset of slugging, the maximum slugging frequency f_{Ms} is an important parameter that also characterizes a deep fluidized bed and is defined as the bubble frequency at which a slug will begin to flow in the bed. The maximum slugging frequency sets a boundary between the bubbling regime and the slugging regime and also offers a secondary confirmation for the onset of slugging regime. In addition, knowledge about the slugging frequency, particularly its maximum value, is important since this parameter can affect the gas−particle contacting. Moreover, as shown in Figure 10, the average bubble diameter over the bed height at the maximum frequency is lower than that characterizing the bed at the minimum slugging velocity. The normalized bubble diameter at the minimum slugging velocity is also the arithmetic mean of the bubble diameters measured

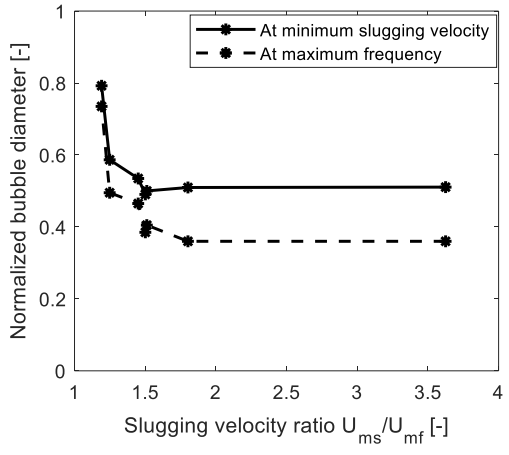

Figure 10. Comparison between bubble diameter at the maximum frequency and that at the minimum slugging velocity for the beds of the glass, limestone, and molecular sieve particles given in Table 1. The bubble diameter for each of the three smaller particles is also averaged over the three different initial bed heights.

DOI: 10.1021/acs.iecr.8b05013
Ind. Eng. Chem. Res. 2019, 58, 2084−2098

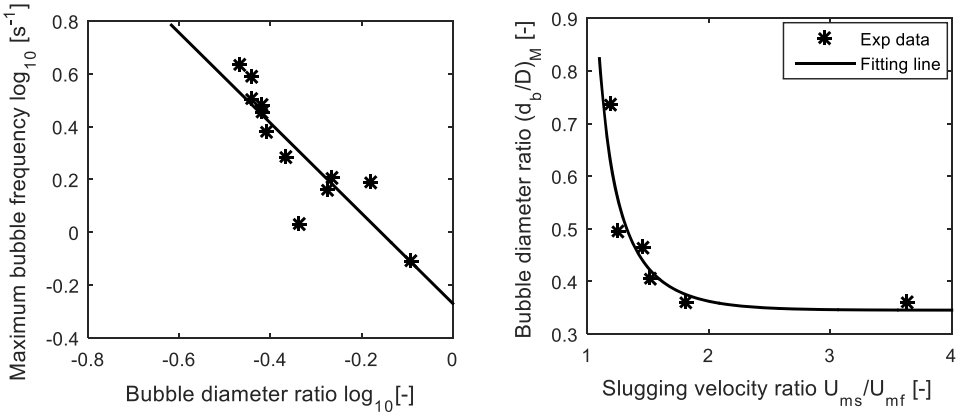

Figure 11. (a) Maximum bubble frequency versus the bubble diameter at this maximum bubble frequency. (b) Bubble diameter at maximum frequency versus minimum slugging velocity ratio for f_{Ms} model development.

from both planes at the minimum slugging velocity since the two measurement planes lie approximately within the middle of the bed for most of the aspect ratios of 4−5.6 covered. This result therefore shows that operating a fluidized bed at the maximum bubble frequency will prevent slugging in a large portion of the bed while achieving higher gas velocity.

From the previous studies,[30−32] different correlations for predicting slugging frequency within the slugging regime are provided. However, there are no such correlations found for the maximum slugging frequency. Based on the analysis of results in this study, a correlation for the maximum slugging frequency can be proposed. It should also be noted that the maximum slugging frequency corresponds to the maximum bubble frequency before the bed begins to slug.

Figure 11(a) shows the plot of $\log_{10}(f_{Ms})$ against the corresponding bubble diameter ratio $\log_{10}(d_b/D)_M$ for the different powders given in Table 1 including glass, limestone, and the molecular sieve particles. The data in the figure also include those obtained from both planes. The result shows that the maximum slugging frequency decreases with the corresponding bubble diameter. As the dependence of bubble frequency on bubble diameter is independent of the bed material,[25] these data can be fitted to a straight line on the log scale with a regression coefficient (R-square) of 0.77. The linear relationship between the maximum slugging frequency and the corresponding bubble diameter can be represented by eq 10.

$$f_{Ms} = k\left(\frac{d_b}{D}\right)_M^{-1.792} \tag{10}$$

where $k = 0.537\ s^{-1}$.

As the local value of $(d_b/D)_M$ is not known, prediction of the local maximum slugging frequency using eq 10 may be difficult. However, using the average of the values of $(d_b/D)_M$ from both planes, an approximate value for the maximum slugging frequency can be obtained. Figure 11(b) shows the plot of average value of $(d_b/D)_M$ against the gas velocity ratio U_{ms}/U_{mf} at the onset of slugging. The bubble diameter decreases with an increasing value of U_{ms}/U_{mf}. The data in the figure can be fitted with a function described by eq 11.

$$(d_b/D)_M = \left(2.90 - 36.66\exp\left(-2.80\frac{U_{ms}}{U_{mf}}\right)\right)^{-1} \tag{11}$$

Combining eqs 10 and 11, the maximum slugging frequency f_{Ms} (s^{-1}) averaged over the bed height can then be expressed as

$$f_{Ms} = 0.537\left(2.90 - 36.66\exp\left(-2.80\frac{U_{ms}}{U_{mf}}\right)\right)^{1.792} \tag{12}$$

Figure 12 compares the prediction of the proposed model for maximum slugging frequency with the experimental data.

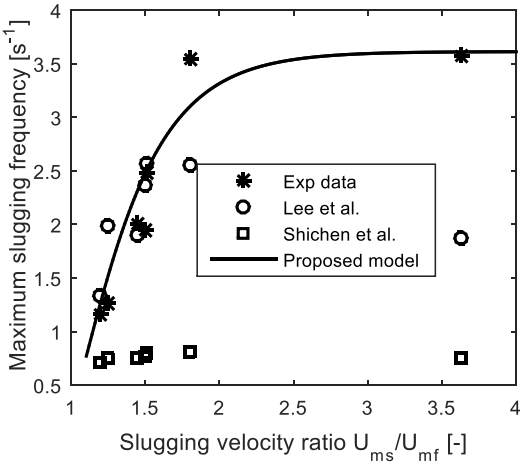

Figure 12. Prediction of maximum slugging frequency using the proposed model compared with results from models in the literature.

The predictions using the correlations given by Lee et al.[30] and Shichen et al.[31] are also shown. The computation of f_{Ms} using the Lee et al. and Shichen et al. correlations are obtained at the superficial gas velocity corresponding to the gas velocity U_{ms} at the onset of slugging. As can be seen, the proposed model, eq 12, predicts the experimental data with reasonable accuracy over a wide range of U_{ms}/U_{mf}. The prediction based on the Lee et al. correlation also agrees with the experimental data for $U_{ms}/U_{mf} < 1.75$. The accuracy of the Lee et al. model in the lower range of U_{ms}/U_{mf} may be due to the range of particle sizes of 450−3000 μm on which the development of the model

DOI: 10.1021/acs.iecr.8b05013
Ind. Eng. Chem. Res. 2019, 58, 2084−2098

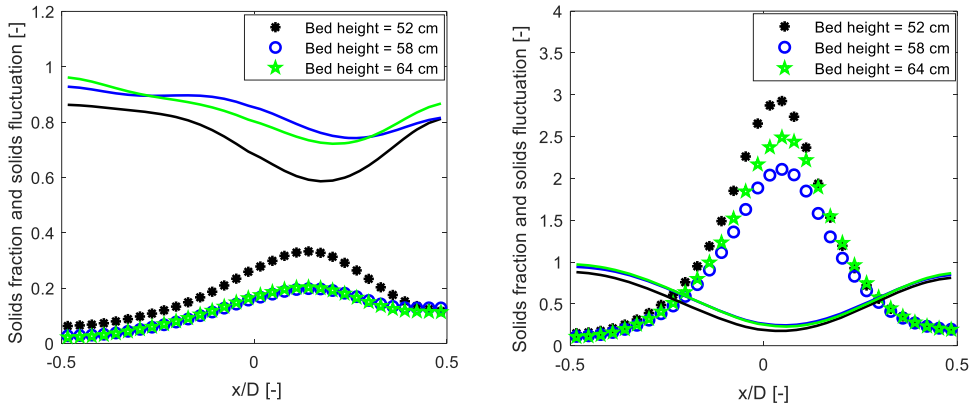

Figure 13. Radial distribution of normalized solids fraction and relative solid fluctuations at the lower planes for the beds of 188 μm glass particles: (a) $U_0 - U_{mf}$ = 0.060m/s. (b) $U_0 - U_{ms}$ = 0.029m/s. Lines: normalized solids fraction. Data points: relative solids fraction fluctuation.

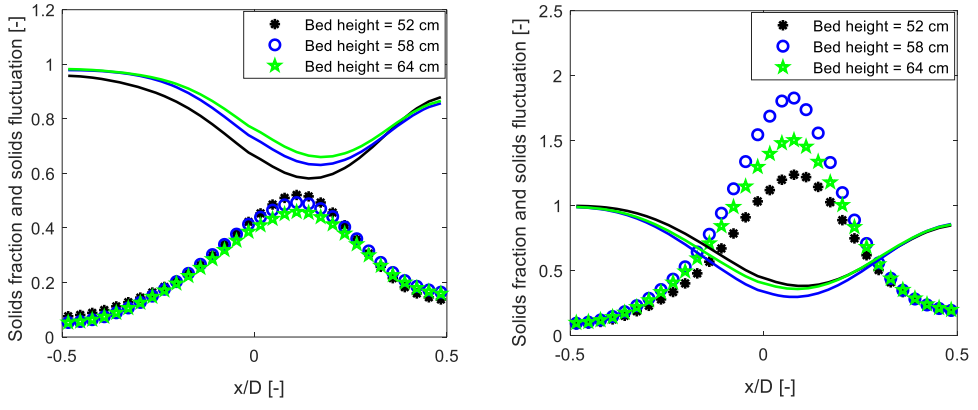

Figure 14. Radial distribution of normalized solids fraction and relative solid fluctuations at the lower planes for the beds of 261 μm glass particles: (a) $U_0 - U_{mf}$ = 0.056m/s and (b) $U_0 - U_{ms}$ = 0.030m/s. Lines: normalized solids fraction. Data points: relative solids fraction fluctuation.

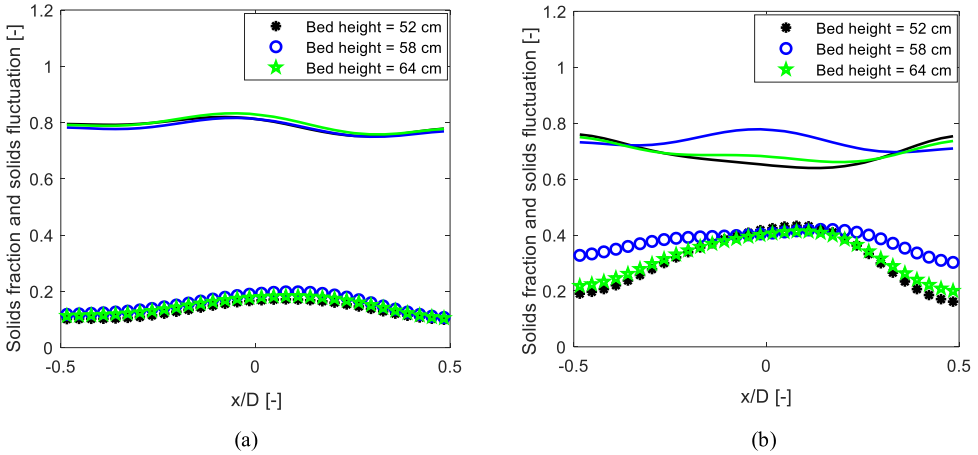

Figure 15. Radial distribution of normalized solids fraction and relative solid fluctuations at the lower planes for the beds of 293 μm limestone particles: (a) $U_0 - U_{mf}$ = 0.058m/s and (b) $U_0 - U_{ms}$ = 0.027m/s. Lines: normalized solids fraction. Data points: relative solids fraction fluctuation.

was based. The Shichen et al. correlation underpredicts the experimental data including those of 697 μm limestone and 624 μm glass particles even though the model was developed based on a particle size of 650 μm. The model might have been developed for a fully developed slug where the slugging frequency approaches 1.0 s^{-1} or less depending on the particles as can be seen in Figure 9, accounting for the inaccuracy in predicting the maximum slugging frequency. Based on these results, the model proposed in this paper can therefore be applied to obtain the maximum bubbling/slugging frequency over a wide range of particle size. Moreover, since the minimum slugging velocity, U_{ms}/U_{mf}, depends on the bed aspect ratio,[3,25] the models given by eqs 11 and 12 can also be

DOI: 10.1021/acs.iecr.8b05013
Ind. Eng. Chem. Res. 2019, 58, 2084−2098

applied in beds of different diameters and heights to a large extent.

4.6. Solids Movement and Distribution of Solids Fraction. In a deep fluidized bed, the higher-pressure drop across the bed may influence the axial bubble distribution. Contrary to shallow beds that are characterized by an even distribution of bubbles, deep beds may be separated into regions of top bubbling zones and regions of bottom quiescent zones. Where a portion of a bed is not bubbling, the solids movement, and thus the required gas−solids mixing in that region, will be jeopardized. The distribution of solids gives an indication of particle mixing in a fluidized bed. Due to bubble formation and passage, the solids are set into oscillate about a fixed position. The degree of movement of solids in the bed at a given gas velocity can be measured by the fluctuations of the solids fraction. The standard deviation of the solids fraction over the measurement period can be used to predict the solids fluctuations in the bed at a given gas velocity. For a given pixel, the standard deviation can be obtained from $\sigma_q = \sqrt{\frac{1}{n-1}\sum(\varepsilon_{sq} - \varepsilon_s)^2}$, where, ε_{sq} is the solids fraction at the pixel $q(i,j)$, and $\varepsilon_s = \frac{1}{n}\sum\varepsilon_{sq}$ is the time average of the solids fraction at that pixel. The indices "i" and "j" locate the pixel in the 32 × 32 plane (Figure 1(b)).

Figures 13, 14, and 15 show the distributions of normalized solids fraction and relative solids fraction fluctuation as a function of the static bed height at the lower plane across the x axis. The normalized solids fraction is obtained from $\varepsilon_{sn} = \varepsilon_s/\varepsilon_{s0}$, while the relative solids fraction fluctuation is computed as $\sigma_{qr} = \sigma_q/\varepsilon_s$, where ε_{s0} is the solids fraction at the fixed state. The value of ε_{sn} ranges from 0 to 1, and it measures the relative permittivity of the solid material. When $\varepsilon_{sn} = 1$, the section of the bed is completely filled with the solid material, but when $\varepsilon_{sn} = 0$, it is completely filled with air. A value in between 0 and 1 means that the bed section is occupied by solids and air. The relative solids fluctuation is used to scale up the effect of gas interactions on the solid particles since $0 < \varepsilon_s \leq 1$, making it easier to compare different bed behavior. The value of σ_{qr} can be less or greater than 1 depending on how severe the gas−solids interaction is. In Figures 13−15, the plots with lines denote the normalized solids fraction, while the data points with the same color represent the corresponding relative solids fraction fluctuation. For each of the beds, two different values of excess velocities are used to compare the effect of particle properties on gas−solids mixing in both bubbling and slugging regimes. For the bubbling regime, the excess velocity above the minimum fluidization velocity $U_0 - U_{mf}$ is kept approximately the same, whereas for the slugging regime the excess velocity above the minimum slugging velocity $U_0 - U_{ms}$ is also approximately the same. The results show that most of the particle movements occur near the center of the beds. The central peak and gradual drop of the solids fluctuations in each bed indicate that particles move upward near the central axis and downward near the walls of the bed in the form of a vortex ring as described in Kunii and Levenspiel[4] for beds of larger diameters. However, there is a significant difference in the bed behavior between the two different materials, glass and limestone particles, at the two different velocities.

For the glass particles, the normalized solids fraction is close to unity near the walls and below unity around the central region, showing that most of the up-flowing gas follows the central axis of the bed. As the bubble rises along the central axis, it pushes the particles by its sides toward the wall and those in its front forward, enhancing gas passage. The emulsion gas tends to follow the region around the central axis due to less resistance to the flow, resulting in the lower solids fraction in this region. When the bubble erupts or coalesces with another bubble, the solids fall back along the sides of the trailing bubble toward the walls. However, as the value of the solids fraction within the central region is below that at the walls, it indicates that only a fraction of the solids carried upward falls back to the plane. This results in an uneven expansion of the bed and slight fluctuations of the solids observed around the wall region. With an increase in the gas velocity, this effect is severe. The region bounded by the central solid movement becomes narrower, increasing the quiescent wall regions. The peak value of the solids fluctuation is high due to passage of slugs. As shown in Figure 5, the passage of the round-nose (axial) slugs increases the wall region due to continuous raining and compression of solids at the sides of the slugs.

For the bed of limestone particles, the distribution of the solids fraction is almost uniform across the bed diameter at the lower gas velocity with the value of ε_{sn} significantly lower than 1.0. This shows that the up-flowing gas is in contact with most of the particles and that the bed expands almost uniformly across the bed cross section. Since the gas distribution is better, the distribution of the solids fraction fluctuation shows that the spread of bubbles is also better than that in the beds of the glass particles. The wider distribution of gas in the limestone bed may be attributed to higher bed porosity due to the nonspherical nature of the particles. At the higher gas velocity, the bed slugs. However, since the rate of occurrence of the flat-face slugs as shown in Figure 5(c) is lower than that of the axial slug shown in Figure 5(b), the fluctuation of the solids fraction in the limestone bed is low compared to that of glass particles at the same excess gas velocity. Figure 15 also shows that as gas velocity is increased, the region bounded by the upward moving particles becomes wider, while the wall region becomes narrower. At this higher gas velocity, the solids fraction distribution is also almost uniform although slightly lower due to an increase in the bed expansion. From these results, it therefore shows that the quality of deep bed fluidization in terms of gas−particles contacting is better in the bed of limestone particles than in that of glass particles.

Moreover, in the bubbling regime, the results clearly show that the effect of bed height on the distributions of solids fraction and solids fluctuation decreases with increasing bed height and with increasing particle size. However, in the slugging regime, the behavior is chaotic. For example, with a bed height 58 cm, the peaks of the solids fluctuation compared to those for the other two heights is the least in the bed of 188 μm glass particles but the greatest in the bed of the larger glass particles. In the bed of limestone particles, the peak values are the same for all the bed heights, but the solids fluctuations spread more evenly at the bed height 58 cm compared to the other heights.

In addition, Figures 13− 15 show that the peak of solids fluctuation is closer to the right wall but shifts toward the central axis as the gas velocity increases. With increasing particle size at the same excess gas velocity, the peak of the fluctuations also moves closer to the central axis due to wider gas distribution. This asymmetric behavior, where the peak of solids fluctuation always lies at the right of the bed central axis, was also observed when the experiments were repeated at the

DOI: 10.1021/acs.iecr.8b05013
Ind. Eng. Chem. Res. 2019, 58, 2084−2098

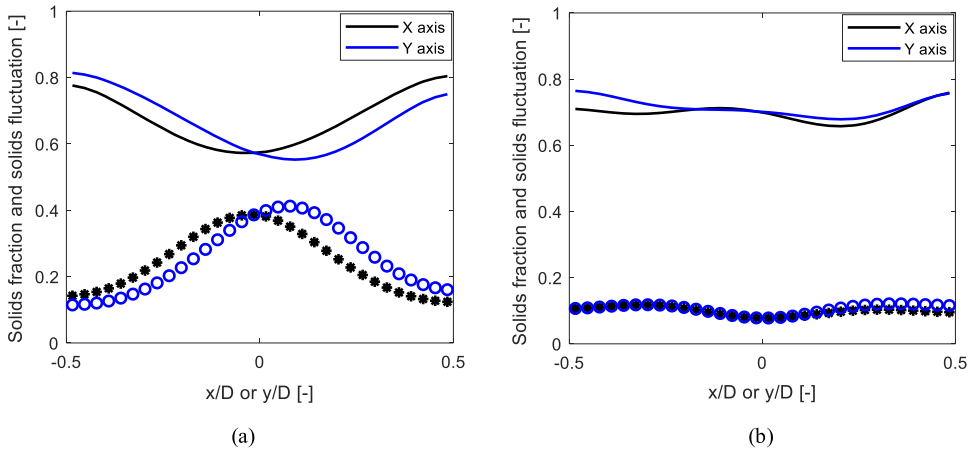

Figure 16. Radial distribution of normalized solids fraction and relative solid fluctuations at the lower planes for the beds of (a) 624 μm glass particles, $U_0 - U_{ms}$ = 0.033m/s, and (b) 697 μm limestone particles, $U_0 - U_{ms}$ = 0.028m/s. Lines: solids fraction. Data points: relative solid fluctuation.

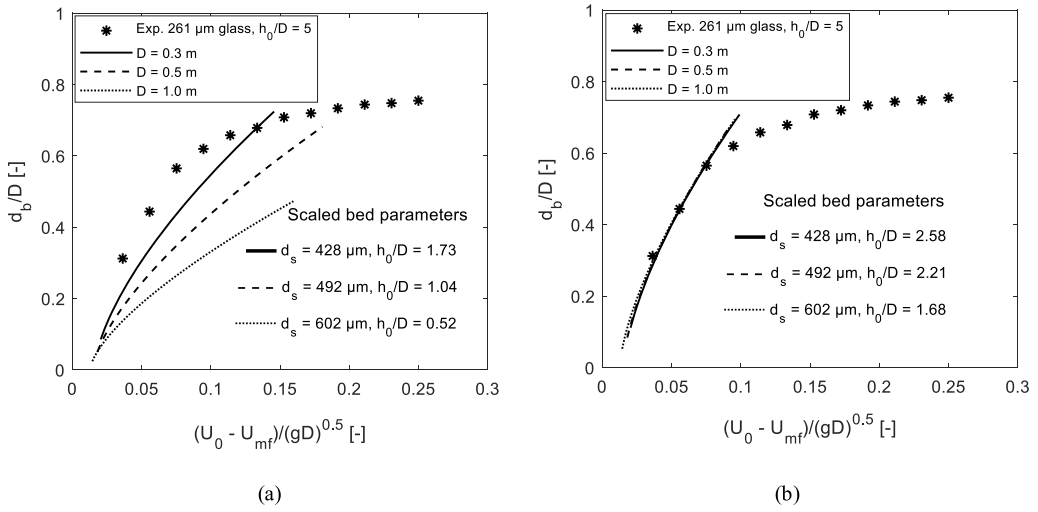

Figure 17. Normalized bubble diameter averaged over a bed height comparing the bubbling behavior in the experimental smaller bed diameter with those in different scaled beds of larger diameters (a) with the same bed height of 52 cm in both experimental and scaled beds and (b) with correctly adjusted bed height for the scaled beds. Scaling laws based on Horio et al.;[34] experimental data and bubble diameter model are as given in Agu et al.[25]

same conditions, indicating a maldistribution of the gas velocity across the bed cross section.

However, the position of the peak of solids fluctuation with respect to the central axis differs between these particles in the *y*-axis (not shown), although the profile of the solids fluctuation as well as the solids fraction is the same as in the *x*-axis. For the higher gas velocity in the *y*-axis, the peak lies at the central axis for the 261 μm glass particles, at the right of the central axis for the 188 μm glass particles, and at the left of the central axis for the limestone particles. When the gas velocity is further increased, the turning points of the solids fraction and fluctuation lie at the central axis in both *x*- and *y*-axes for all the particles, indicating an even distribution of gas/bubbles across the bed. The variation in the orientation of the solids fraction and fluctuation between the *x*- and *y*-axes can be seen clearly in Figure 16 for the beds of 624 μm glass and 697 μm limestone particles at $U_0 - U_{ms} \approx 0.03$m/s. The results also show that the peak of the solids fluctuation lies at different positions between the *x*- and *y*-axes for the glass particles but at the same position in both *x*- and *y*-axes for the limestone particles.

Since the position of the peak of solids fluctuations in either the *x*- or *y*-axis depends on both particle size and gas velocity, the distribution of bubbles in the bed might have also been influenced by the distributor plate. As can be seen in Figure 2, the ratio of the distributor pressure to the bed pressure drop is very low for smaller particles and high for larger particles at the same gas velocity ratio. Increasing the gas velocity increases the distributor pressure drop. With a sufficiently high pressure drop across the distributor, a large number of pores on the plate are active to give a better gas distribution.[4] The maldistribution of the gas velocity from the distributor plate, particularly in the bed of smaller particle sizes, can be minimized by adding a packed bed or porous medium in the plenum below the distributor plate. It should be noted that in this study the distributor pressure drop was kept low to be able to operate all the beds within the range of gas velocities covered since the maximum pressure drop across the air blower is 0.15 bar(g).

4.7. Modeling and Scale-Up. From the results obtained in this study, different correlations for different bubble

DOI: 10.1021/acs.iecr.8b05013
Ind. Eng. Chem. Res. 2019, 58, 2084−2098

properties have been proposed.[25,27] In Agu et al.,[27] models for the bubble velocity, bubble frequency, and bed expansion were presented, while the models for the bubble volumetric flux and bubble diameter averaged over the bed height were proposed in Agu et al.[25] The bubble frequency and bubble diameter models are as given in eqs 13 and 14, respectively.

$$f_b = \left(0.52\left(\frac{d_b}{D}\right)^{1.48} + \gamma u_b^{\beta} d_b\right)^{-1} \tag{13}$$

$$\bar{d}_b/D = 0.848\left(\frac{U_0}{D}\right)^{0.66}\left(1 - c\left(\frac{U_0}{U_{mf}}\right)^{a-1}\right)^{0.66} \tag{14}$$

where u_b is the bubble velocity. All the model parameters γ, β, a, and c depend on whether the bed is in bubbling or slugging regime. While γ and β depend on the particle class, a and c depend on the particle and fluid properties as described in the respective literature. These two models can accurately predict the results presented in this study for different gas velocities, particle sizes, and flow regimes.

As shown in previous sections, different particle types behave differently in the 10.4 cm diameter bed used in this study at their respective initial bed heights. In a larger bed diameter, the behavior shown by the same particles may differ due to higher degrees of freedom in both particle and bubble flows. To obtain a similarity in the behavior shown by any of the powders, a correctly scaled bed of another particle type is required. There are several scaling laws in the literature[33] for achieving a similarity in the fluidized bed behavior between smaller and larger diameter beds. For simplicity, the dimensionless group described in eq 15 as proposed by Horio et al.[34] for attaining a similarity in a bubbling bed is used for a demonstration.

$$\frac{U_0 - U_{mf}}{\sqrt{gD}}, \frac{U_{mf}}{\sqrt{gD}}, \frac{\rho_g}{\rho_s} \tag{15}$$

For the 261 μm glass particles in the bed of dimeter 10.4 cm and initial height 52 cm, for example, Figure 17 shows the behavior when the bed is scaled to larger bed diameters, 30, 50, and 100 cm, using the scaling dimensionless group given in eq 15. The experimental data are the normalized bubble diameter $\bar{d}_b/D$ averaged over the bed height at different gas velocities. The values of $\bar{d}_b/D$ for the scaled beds are determined from eq 14. For the same particle density and air properties, the particle diameter in the scaled bed is obtained by back calculation from the Wen and Yu[35] correlation proposed for predicting the minimum fluidization velocity of a known fluid and particle properties. When the bed height is 52 cm, giving the aspect ratios h_0/D = 1.73, 1.04, and 0.52 for the respective bed diameters, Figure 17(a) shows that there is no similarity between the scaled and the experimental beds. The bubble diameter decreases with decreasing bed aspect ratio, reflecting a characteristic behavior of shallow beds. To match the normalized bubble diameter from the scaled bed to that of the experimental bed, the bed aspect ratio has to be increased as shown in Figure 17(b). The new bed aspect ratio is given as h_{0*}/D_*, where h_{0*} = 52 cm and D_* is a characteristics scaling bed diameter obtained by fitting eq 14 for a given scaled particle properties to the experimental data from the small scale bed. It should also be noted that the similarity attained is only within the bubbling regime as can be seen in Figure 17(b). To achieve a similar behavior in the slugging regime, a different set of scaling dimensionless groups may be applied.

From these results, it therefore shows that the bubbling bed behavior observed in this study can be scaled up using appropriate scaling laws in addition to eq 14.

5. CONCLUSIONS

In this paper, a number of experiments were carried out to deepen the understanding of influence of particle properties and bed height on the behavior of deep bubbling fluidized beds. The powders including limestone, glass, sand, and molecular sieve particles with mean particle sizes in the range of 180−2200 μm were investigated. The bed height was varied between 50 and 65 cm in a 10.4 cm diameter cylindrical bed. The bubble properties were obtained at two different positions in the bed using the information acquired by a dual-plane ECT sensor.

The results show that particle properties influence the bubbling behavior and that the effect of bed height depends on the particle size. The findings of this study are summarized as follows:

- Bubbles grow faster in the bed of limestone particles than in that of glass particles, possibly due to variation in their shapes that influences the bed porosity.
- The rate of bubble growth increases with increasing particle size, basically due to low resistance to gas flow in the bed of larger particles.
- Bubble frequency increases with gas velocity only when the bubble diameter is below a threshold value. At the threshold bubble diameter, the bubble frequency is maximum, and above the threshold value, the bubble frequency decreases with increasing gas velocity.
- The bubble diameter at the maximum bubble frequency increases with increasing particle size.
- When the bubble diameter reaches a value at which the bubble frequency is maximum, the bed begins to slug.
- For rough particles, the slug type can change from flat slugs to wall slugs depending on the gas velocity and axial position in the bed.
- The limiting slug frequency is closer to or less than 1.0 s^{-1} for large or rough particles but may be higher for small and smooth particles.
- Correlations for predicting average maximum bubble frequency and the corresponding bubble diameter are proposed.
- Gas−solid contacting is more effective at higher gas velocity in the bed of limestone particles than in that of glass particles.
- The effect of bed height decreases with increasing aspect ratio within the bubbling regime but may vary within the slugging regime due to the chaotic behavior of slug flows.

With the findings in this paper, understanding of bubbling behavior in deep fluidized beds is enhanced for efficient operations and designs of such systems. The effect of different particle size distributions and gas distributors on deep bed behavior will be considered in further studies.

AUTHOR INFORMATION

Corresponding Author

*E-mail: cornelius.e.agu@usn.no.

DOI: 10.1021/acs.iecr.8b05013
Ind. Eng. Chem. Res. 2019, 58, 2084−2098

ORCID

Cornelius E. Agu: 0000-0002-5339-9794
Christoph Pfeifer: 0000-0002-7747-9297

Funding

This research did not receive any specific grant from funding agencies in the public, commercial, or not-for-profit sectors.

Notes

The authors declare no competing financial interest.

NOMENCLATURE SYMBOLS

A [m^2] = cross-sectional area
D [m] = bed diameter
D_* [m] = characteristic scaled bed diameter
d [m] = diameter
f_b [1/s] = bubble frequency
g [m/s^2] = acceleration due to gravity
H [m] = total bed height
h [m] = vertical position in the bed
h_{0*} [m] = initial bed height for this small bed diameter of 10.4 cm
n [-] = number
T [s] = period
U,u [m/s] = velocity

GREEK LETTERS

ε_s [-] = solids fraction
ρ [kg/m^3] = density
σ [-] = solids fraction standard deviation

SUBSCRIPTS

b = bubble
ba = active bubble
f = fluidized
i = idle/index
M = maximum
mf = minimum fluidization
q = pixel
s = slug/solid
0 = initial/bottom reference

REFERENCES

(1) Toomey, R. D.; Johnstone, H. F. Gaseous fluidization of solid particles. *Chem. Eng. Prog.* **1952**, *48*, 220.
(2) Grace, J. R. Contacting modes and behaviour classification of gas-solid and other two-phase suspensions. *Can. J. Chem. Eng.* **1986**, *64*, 353.
(3) Baeyens, J.; Geldart, D. An investigation into slugging fluidized beds. *Chem. Eng. Sci.* **1974**, *29*, 255.
(4) Kunii, D.; Levenspiel, O. *Fluidization Engineering*, second ed.; Butterworth−Heinemann: Oxford, U.K., 1991.
(5) Gupta, C. K.; Sathiyamoorthy, D. *Fluid Bed Technology in Materials Processing*, first ed.; CRC Press: Boca Raton, FL, 1999.
(6) Wang, T.; He, Y.; Tang, T.; Zhao, Y. Numerical investigation of particle behaviour in a bubbling fluidized bed with non-spherical particles using discrete hard sphere method. *Powder Technol.* **2016**, *301*, 927.
(7) Verma, V.; Padding, J. T.; Deen, N. G.; Kuipers, J. A. M. Effect of bed size on hydrodynamics in 3-D gas-solid fluidized beds. *AIChE J.* **2015**, *61*, 1492.
(8) Verma, V.; Padding, J. T.; Deen, N. G.; Kuipers, J. A. M.; Barthel, F.; Bieberle, M.; Wagner, M.; Hampel, U. Bubble dynamics a in 3-D gas-solid fluidized bed using ultrafast electron beam X-ray tomography and two-fluid model. *AIChE J.* **2014**, *60*, 1632.
(9) Laverman, J. A.; Roghair, I.; Annaland, M. V. S.; Kuipers, H. Investigation into the hydrodynamics of gas-solid fluidized beds using particle image velocimetry coupled with digital image analysis. *Can. J. Chem. Eng.* **2008**, *86*, 523.
(10) Wang, D.; Xu, M.; Marashdeh, Q.; Straiton, B.; Tong, A.; Fan, L.-S. Electrical capacitance volume tomography for characterization of gas-solid slugging fluidization with Geldart group D particles under high temperatures. *Ind. Eng. Chem. Res.* **2018**, *57*, 2687.
(11) Cho, H.; Han, G.; Ahn, G. Characteristics of slug flow in a fluidized bed of polyethylene particles. *Korean J. Chem. Eng.* **2002**, *19*, 183.
(12) Raghuraman, J.; Potter, O. E. Modeling the Slugging Fluidized Bed Reactor. In *Chemical Reaction Engineering − Houston*; Vern, W.; Weekman, Jr.; Dan, L., Eds.; ACS Symposium Series *65*, 1978; pp 400−410.
(13) van Ommen, J. R.; Mudde, R. F. Measuring the gas-solids distribution in fluidized beds − A review. *Int. J. Chem. React. Eng.* **2008**, *6*, 1.
(14) Rautenbach, C.; Mudde, R. F.; Yang, X.; Melaaen, M. C.; Halvorsen, B. M. A comparative study between electrical capacitance tomography and time-resolved X-ray tomography. *Flow Meas. Instrum.* **2013**, *30*, 34.
(15) Nguyen, X. T.; Leung, L. S. A note on bubble formation at an orifice in a fluidized bed. *Chem. Eng. Sci.* **1972**, *27*, 1748.
(16) Verloop, J.; Heertjes, P. M. Periodic pressure-fluctuations in fluidized-beds. *Chem. Eng. Sci.* **1974**, *29*, 1035.
(17) Choi, J. H.; Son, J. E.; Kim, S. D. Bubble size and frequency in gas fluidized beds. *J. Chem. Eng. Jpn.* **1988**, *21*, 171.
(18) Mori, S.; Wen, C. Y. Estimation of bubble diameter in gaseous fluidized beds. *AIChE J.* **1975**, *21*, 109.
(19) Darton, R. C.; La Naueza, R. D.; Davidson, J. F.; Harrison, D. Bubble growth due to coalescence in fluidized beds. *Trans. Inst. Chem. Eng.* **1977**, *55*, 274.
(20) Cai, P.; Schiavetti, M.; De Michele, G. D.; Grazzini, G. C.; Miccio, M. Quantitative estimation of bubble size in PFBC. *Powder Technol.* **1994**, *80*, 99.
(21) Karimipour, S.; Pugsley, T. A critical evaluation of literature correlations for predicting bubble size and velocity in gas-solid fluidized beds - A review. *Powder Technol.* **2011**, *205*, 1.
(22) Geldart, D. Types of gas fluidization. *Powder Technol.* **1973**, *7*, 285.
(23) Agu, C. E.; Tokheim, L.-A.; Eikeland, M.; Moldestad, B. M.E. Determination of onset of bubbling and slugging in a fluidized bed using a dual-plane electrical capacitance tomography system. *Chem. Eng. J.* **2017**, *328*, 997.
(24) *Electrical Capacitance Tomography System. Operating Manual Vol. 1: Fundamentals of ECT*; Process Tomography Ltd., 2009.
(25) Agu, C. E.; Pfeifer, C.; Eikeland, M.; Tokheim, L.-A.; Moldestad, B. M.E. Models for predicting average bubble diameter and volumetric bubble flux in deep fluidized beds. *Ind. Eng. Chem. Res.* **2018**, *57*, 2658.
(26) Weber, J. M.; Mei, J. S. Bubbling fluidized bed characterization using electrical capacitance volume tomography (ECVT). *Powder Technol.* **2013**, *242*, 40.
(27) Agu, C. E.; Tokheim, L.-A.; Eikeland, M.; Moldestad, B. M.E. Improved models for predicting bubble velocity, bubble frequency and bed expansion in a bubbling fluidized bed. *Chem. Eng. Res. Des.* **2019**, *141*, 361.
(28) Lu, Y.; Huang, J.; Zheng, P. A CFD-DEM study of bubble dynamics in fluidized bed using flood fill method. *Chem. Eng. J.* **2015**, *274*, 123.
(29) Werther, J. Bubble Growth in Large Diameter Fluidized Beds. In *Fluidization Technology*; Keairns, D. L., Eds.; Hemisphere Publishing Corporation: Washington, DC, 1976; pp 216−235.
(30) Lee, S. H.; Lee, D. H.; Kim, S. D. Slug characteristics of polymer particles in a gas-solid fluidized bed. *Korean J. Chem. Eng.* **2002**, *19*, 351.

DOI: 10.1021/acs.iecr.8b05013
Ind. Eng. Chem. Res. 2019, 58, 2084−2098

(31) Shichen, C.; Heling, Z.; Feichen, J. A Study of Hydrodynamics Behaviour of the Slugging Fluidized Bed. In *Fluidization*; Kwauk, M. K.; Kunii, D., Eds.; Elsevier: Amsterdam, 1985; pp 75−85.
(32) Noordergraaf, I. W.; VanDijk, A.; Van Den Bleek, C. M. Fluidization and slugging in large-particle systems. *Powder Technol.* **1987**, *52*, 59.
(33) Rudisuli, M.; Schildhauer, T. J.; Biollaz, S. M. A.; van-Ommen, J. R. Scale-up of bubbling fluidized bed reactors − A review. *Powder Technol.* **2012**, *217*, 21.
(34) Horio, M.; Nonaka, A.; Sawa, I.; Muchi, Y. A new similarity rule for fluidized bed scale-up. *AIChE J.* **1986**, *32*, 1466.
(35) Wen, C. Y.; Yu, Y. H. A Generalized Method for Predicting the Minimum Fluidization Velocity. *AIChE J.* **1966**, *12*, 610.

DOI: 10.1021/acs.iecr.8b05013
Ind. Eng. Chem. Res. 2019, 58, 2084−2098